The Monitor project: rotation of low-mass stars in NGC 2362 – testing the disc regulation paradigm at 5 Myr

Jonathan Irwin,[1,2]★ Simon Hodgkin,[1] Suzanne Aigrain,[3] Jerome Bouvier,[4] Leslie Hebb,[5] Mike Irwin[1] and Estelle Moraux[4]

[1]*Institute of Astronomy, University of Cambridge, Madingley Road, Cambridge CB3 0HA*
[2]*Harvard–Smithsonian Center for Astrophysics, 60 Garden Street, Cambridge, MA 02138, USA*
[3]*Astrophysics Group, School of Physics, University of Exeter, Stocker Road, Exeter EX4 4QL*
[4]*Laboratoire d'Astrophysique, Observatoire de Grenoble, BP 53, F-38041 Grenoble Cedex 9, France*
[5]*School of Physics and Astronomy, University of St Andrews, North Haugh, St Andrews KY16 9SS*

ABSTRACT

We report on the results of a time-series photometric survey of NGC 2362, carried out using the CTIO 4-m Blanco telescope and Mosaic-II detector as part of the Monitor project. Rotation periods were derived for 271 candidate cluster members over the mass range $0.1 \lesssim M/M_\odot \lesssim 1.2$. The rotation period distributions show a clear mass-dependent morphology, qualitatively similar to that in NGC 2264, as would be expected from the age of this cluster. Using models of angular momentum evolution, we show that angular momentum losses over the $\sim$1–5 Myr age range appear to be needed in order to reproduce the evolution of the slowest rotators in the sample from the ONC to NGC 2362, as found by many previous studies. By incorporating *Spitzer* IRAC mid-infrared (mid-IR) measurements, we found that three to four objects showing mid-IR excesses indicative of the presence of circumstellar discs were all slow rotators, as would be expected in the disc regulation paradigm for early pre-main-sequence angular momentum evolution, but this result is not statistically significant at present, given the extremely limited sample size.

Key words: techniques: photometric – surveys – stars: pre-main-sequence – stars: rotation – open clusters and associations: individual: NGC 2362.

1 INTRODUCTION

NGC 2362 is a very young open cluster, at a moderate distance. We adopt the parameters of Moitinho et al. (2001) for the remainder of this work: an age of 5^{+1}_{-2} Myr, distance 1480 pc and reddening $E(B-V) = 0.10$ mag. Note however that there is some controversy in the literature regarding the age of this cluster, with estimates ranging from 3–9 Myr. Mayne et al. (2007) have examined the relative ages of young open clusters, finding that NGC 2362 does indeed seem to be older than the ONC, but that it may be younger than IC 348, and they suggest an age of $\sim$3 Myr.

Nevertheless, the extremely young age, and lack of substantial nebulosity or differential reddening in this cluster make it an ideal testing ground for theories of pre-main-sequence (PMS) stellar evolution. Dahm (2005) carried out an extensive spectroscopic survey, concentrating on the Hα 6563 Å and Li I 6707.8 Å features, finding that a large fraction ($\sim$91 per cent) of the T Tauri star (TTS) population in NGC 2362 is composed of weak-line emitters (WTTS), as

expected given the canonical 5 Myr age for the cluster. They found that $\sim$5–9 per cent of the TTS population are likely to still be undergoing accretion on the basis of the measured Hα equivalent widths, which is comparable to the fraction of objects found to exhibit *L*-band excess emission indicative of an inner disc by Haisch, Lada & Lada (2001).

NGC 2362 has also been observed more recently with *Spitzer* using the IRAC (Infrared Array Camera) instrument in the 3.6, 4.5, 5.8 and 8.0 µm bands. Dahm & Hillenbrand (2007) used these observations to derive spectral energy distributions (SEDs) for candidate NGC 2362 members, and to characterize disc emission in objects exhibiting infrared (IR) excesses. They found an upper limit to the fraction of objects exhibiting optically thick discs of $\sim$7 $\pm$ 2 per cent, with an additional $\sim$12 $\pm$ 3 per cent of objects exhibiting weak or optically thin discs.

1.1 Evolution of stellar angular momentum

A long-standing issue in our understanding of the evolution of stellar rotation rates on the PMS is that significant loss of angular

★E-mail: jmi@ast.cam.ac.uk

momentum appears to be required in order to reproduce the observed rotation rates of low-mass stars.

During the first few Myr of their evolution, low-mass PMS stars contract by factors of $\sim$2–3. Hence, if angular momentum is conserved, all subsolar mass stars, which are thought to have initial rotation periods of $\sim$10 d, should rotate at periods shorter than 2 d after only 2–3 Myr. Observations at these ages show that some stars rotate much slower than this rate, and indeed the slowest rotators do not appear to spin up at all over the first few Myr of their evolution.

The most popular scenarios for solving this problem invoke additional angular momentum losses resulting from the interaction of the star with a circumstellar disc (e.g. König 1991). In the 'disc locking' scenario, this interaction results in transfer of angular momentum from the star to the disc, which maintains a constant stellar rotation rate until the disc dissipates sufficiently to break the coupling. Alternatively, the angular momentum may be lost through an enhanced stellar wind, powered by the accretion of material from the disc (Matt & Pudritz 2005).

In both cases, the most basic prediction of the models is that there should be a correlation between rotation rate and the presence of discs, in the sense that the slow rotators should still be surrounded by discs, whereas for the rapid rotators, the discs should have dispersed.

Much of the recent literature on rotation has been devoted to the search for a correlation between rotation rate and disc indicators, including diagnostics of accretion (ultraviolet excess, spectral line diagnostics such as Hα, etc.) and of the thermal emission from the disc itself (IR excess). Many of the early studies were inconclusive, due to a combination of effects including small sample sizes, biases, dependence of the adopted disc indicators on other stellar parameters (predominantly mass), and the use of ambiguous disc indicators.

Two recent studies (Rebull et al. 2006; Cieza & Baliber 2007) have claimed statistically significant detections of the expected correlation between slow rotators and circumstellar discs, in the ONC (1 $\pm$ 1 Myr; Hillenbrand 1997) and NGC 2264 (2–4 Myr; Park et al. 2000), respectively. Cieza & Baliber (2006) have also examined IC 348 (2–3 Myr; Luhman et al. 2003), but the results were ambiguous due to small number statistics. These studies have all used the IRAC instrument on the *Spitzer Space Telescope*, which provides mid-IR photometry in four broad-bands: 3.6, 4.5, 5.8 and 8.0 μm. In particular, 8.0 μm IR flux excesses provide a much more reliable indicator of the presence of circumstellar discs than shorter wavelength IR excesses (e.g. in the K band). There is thus mounting evidence in favour of the disc regulation paradigm, but nevertheless, it is important to verify that this result extends to older open clusters.

1.2 The survey

We have undertaken a photometric survey in NGC 2362 using the CTIO 4-m Blanco telescope and Mosaic-II imager. Our goals are twofold: first, to study rotation periods for a sample of low-mass members, covering K and M spectral types, down to $\sim$0.1 M$_\odot$, and secondly, to look for eclipsing binary systems containing low-mass stars, to obtain dynamical mass measurements in conjunction with radial velocities from follow-up spectroscopy. Such systems provide the most accurate determinations of fundamental stellar parameters (in particular, masses) for input to models of stellar evolution, which are poorly constrained in this age range. We defer discussion of our search for occultations to another publication (Miller et al., 2008).

These observations are part of a larger photometric monitoring survey of young open clusters over a range of ages and metallicities (the Monitor project; Hodgkin et al. 2006 and Aigrain et al. 2007).

The remainder of the paper is structured as follows. The observations and data reduction are described in Section 2, and the colour–magnitude diagram (CMD) of the cluster and candidate membership selection are presented in Section 3. The method we use for obtaining photometric periods is summarized in Section 4 (see Irwin et al. 2006 for a more detailed discussion). Our results are given in Section 5, and Section 6 summarizes our conclusions.
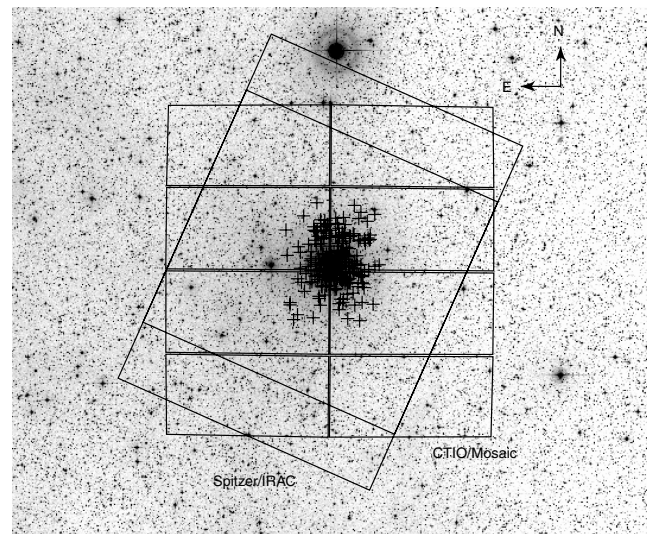
In several of the following sections, we use mass and radius estimates for the cluster members. These were derived from the 5 Myr NEXTGEN models, using the I-band magnitudes, rather than $V - I$ colour or V magnitude, for reasons discussed in Section 3.1.
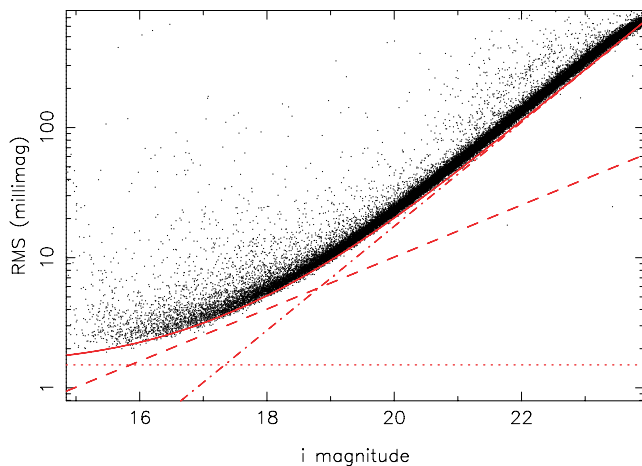
2 OBSERVATIONS AND DATA REDUCTION

Photometric monitoring observations were obtained using the 4-m CTIO Blanco telescope, with the Mosaic-II imager, on 8 $\times$ 1/2-nights between 2005 December 24 and 2006 January 06. This instrument provides a field of view (FOV) of $\sim$36 $\times$ 36 arcmin^2 (0.37 deg^2), using a mosaic of eight 2048 $\times$ 4096 pixel CCDs, at a scale of $\sim$ 0.27 *arcsec* pix^{-1}.

A single field in NGC 2362, centred on the star τ CMa (see Fig. 1), was observed for $\sim$ 4 h per night, in parallel with another field in the cluster M50, the results from which will be published separately. Exposure times were 75 s in i band, giving a cadence of $\sim$6 minutes (composed of 2 $\times$ 75 s exposures plus 2 $\times$ 100 s readout time, slewing between M50 and NGC 2362 during readout). We also obtained deep V-band exposures (600, 450, 2 $\times$ 300 and 150 s) which were stacked and used to produce a CMD of the cluster.

For a full description of our data reduction steps, the reader is referred to Irwin et al. (2007a). Briefly, we used the pipeline for the INT wide-field survey (Irwin & Lewis 2001) for 2D instrumental signature removal (bias correction, flat-fielding, defringing) and astrometric and photometric calibration. We then generated a

Figure 1. Digitized sky survey image of NGC 2362 covering $\sim$1°2 $\times$ 1°, showing the coverage of the present survey (eight-chip mosaic tile), and the *Spitzer* IRAC field of Dahm & Hillenbrand (2007), showing the total coverage (larger box), and the smaller central region covered by all four bands. Crosses show the positions of the candidate cluster members from Dahm & Hillenbrand (2007).

Figure 2. Plot of rms scatter per data point (measured over the entire data set of 8 × 1/2-nights) as a function of magnitude for the *i*-band observations of a single field in NGC 2362, for all unblended objects with stellar morphological classifications. The diagonal dashed line shows the expected rms from Poisson noise in the object, the diagonal dot–dashed line shows the rms from sky noise in the photometric aperture, and the dotted line shows an additional 1.5 mmag contribution added in quadrature to account for systematic effects. The solid line shows the overall predicted rms, combining these contributions.

master catalogue for each filter by stacking 20 of the frames taken in the best conditions (seeing, sky brightness and transparency) and running the source detection software on the stacked image. The resulting source positions were used to perform aperture photometry on all of the time-series images. We achieved a per data point photometric precision of ∼2–4 mmag for the brightest objects, with rms scatter <1 per cent for $i \lesssim 19$ (see Fig. 2). A signal-to-noise ratio of 5 (corresponding approximately to the detection limit for point sources on a single frame of the differential photometry) is reached at $i \sim 22.7$.

Our source detection software flags any objects detected as having overlapping isophotes. This information is used, in conjunction with a morphological image classification flag also generated by the pipeline software (Irwin & Lewis 2001) to allow us to identify non-stellar or blended objects in the time-series photometry.

Photometric calibration of our data was carried out using regular observations of Landolt (1992) equatorial standard star fields in the usual way.

Light curves were extracted from the data for ∼85 000 objects, 56 000 of which had stellar morphological classifications (∼40 per cent of these are flagged as blended), using our standard aperture photometry techniques, described in Irwin et al. (2007a). We fit a 2D quadratic polynomial to the residuals in each frame (measured for each object as the difference between its magnitude on the frame in question and the median calculated across all frames) as a function of position, for each of the eight CCDs separately. Subsequent removal of this function accounts for effects such as varying differential atmospheric extinction across each frame. Over a single CCD, the spatially varying part of the correction remains small, typically ∼0.02 mag peak-to-peak. The reasons for using this technique are discussed in more detail in Irwin et al. (2007a).

For the production of deep CMDs, we stacked 20 *i*-band observations, taken in good seeing and photometric conditions, and all of the *V*-band observations. The limiting magnitudes on these stacked images, measured as the approximate magnitude at which our catalogues are 50 per cent complete, were $V \simeq 24.4$ and $i \simeq 23.6$.
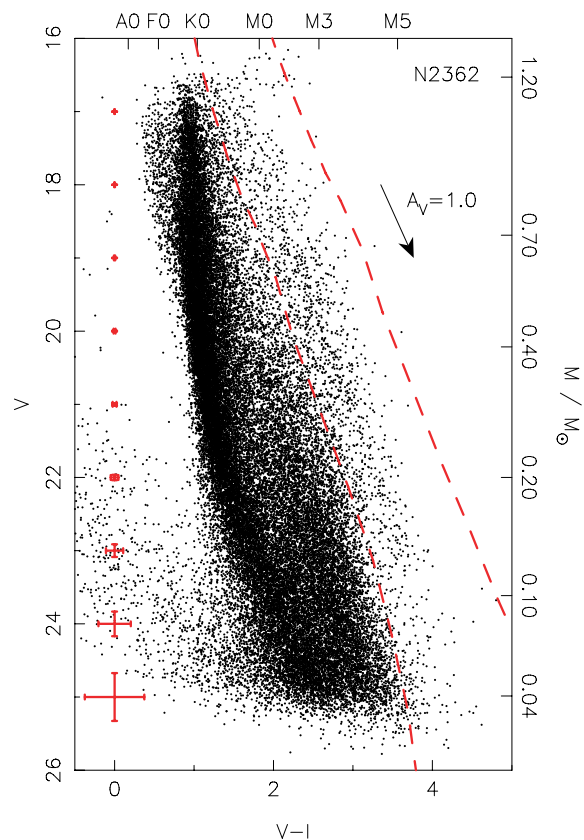
3 SELECTION OF CANDIDATE LOW-MASS MEMBERS

Catalogues of candidate NGC 2362 members are available in the literature (Moitinho et al. 2001; Dahm 2005), but we elected to perform a new photometric selection using *V* versus *V − I* CMDs from our data in order to properly match the relatively large FOV of our time-series observations compared to these previous studies.

3.1 The *V* versus *V − I* CMD

Our CMD of NGC 2362 is shown in Fig. 3. The *V* and *i* measurements were converted to the standard Johnson–Cousins photometric system using colour equations derived from our standard star observations:

$$(V - I) = (V_{ccd} - i_{ccd})/0.899, \tag{1}$$

Figure 3. *V* versus *V − I* CMD of NGC 2362 from stacked images, for all objects with stellar morphological classification. The cluster sequence is clearly visible on the right-hand side of the diagram. The boundaries of the region used to select photometric candidate members are shown by the dashed lines (all objects between the dashed lines were selected). The reddening vector for $A_V = 1.0$ is shown at the right-hand side of the diagram. The mass scale is from the 5 Myr NEXTGEN models (Baraffe et al. 1998) for $M > 0.1 \, M_\odot$, and the 5 Myr DUSTY models (Chabrier et al. 2000) for $M < 0.1 \, M_\odot$, using our empirical isochrone to convert the *V* magnitudes to *I* magnitudes, and subsequently obtaining the masses from these, due to known problems with the *V* magnitudes from the models (see Section 3.1). The error bars at the left-hand side of the plot indicate the typical photometric error for an object on the cluster sequence.

$$V = V_{ccd} + 0.005\,(V - I), \qquad (2)$$

$$I = i_{ccd} - 0.096\,(V - I). \qquad (3)$$

Candidate cluster members were selected by defining an empirical cluster sequence 'by eye' to follow the clearly visible cluster single-star sequence. The cuts were defined by moving this line along a vector perpendicular to the cluster sequence, by amounts $k - \sigma(V - I)$ and $k + \sigma(V - I)$ as measured along this vector, where $\sigma(V - I)$ is the photometric error in the $V - I$ colour. The values of k used were -0.25 mag for the lower line and 0.7 mag for the upper line on the diagram, making the brighter region wider to avoid rejecting binary and multiple systems, which are overluminous for their colour compared to single stars. 1800 candidate photometric members were selected, over the full V magnitude range from $V = 16$–26, but the well-defined cluster sequence appears to terminate at $M \sim 0.1\,M_\odot$, or $V \sim 23.5$, with a few candidate brown dwarfs found below this limit, but with high field contamination.

We also considered using the model isochrones of Baraffe et al. (1998) and Chabrier et al. (2000) for selecting candidate members. The NEXTGEN model isochrones were found to be unsuitable due to the known discrepancy between these models and observations in the $V - I$ colour for $T_{eff} \lesssim 3700$ K (corresponding here to $V - I \gtrsim 2$). This was examined in more detail by Baraffe et al. (1998), and is due to a missing source of opacity at these temperatures, leading to overestimation of the V-band flux. Consequently, when we have used the NEXTGEN isochrones to determine model masses and radii for our objects, the I-band absolute magnitudes were used to perform the relevant look-up, since these are less susceptible to the missing source of opacity, and hence give more robust estimates.
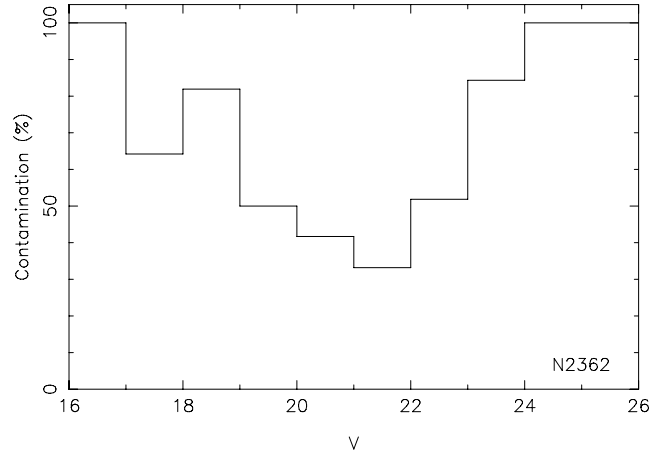
3.2 Contamination

Since the cluster sequence is not well separated from the field in the CMD, it is important to estimate the level of field star contamination in the sample of candidate cluster members. This has been done using two independent methods.
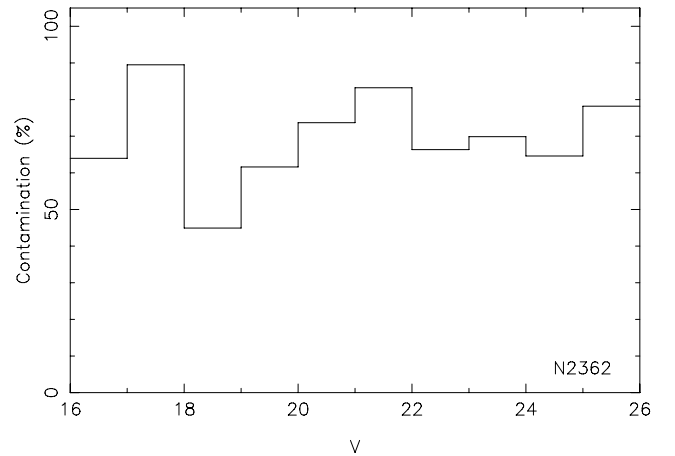
3.2.1 Galactic models

The Besançon Galactic models (Robin et al. 2003) were used to generate a simulated catalogue of objects passing our selection criteria at the Galactic coordinates of NGC 2362 ($l = 238°.2$, $b = -5°.5$), covering the total FOV of ~ 0.35 deg^2 (including gaps between detectors). The same selection process as above for the cluster members was applied to this catalogue to find the contaminant objects. A total of 1500 simulated objects passed these membership selection criteria, giving an overall contamination level of ~ 65 per cent after correcting for bins where the number of objects predicted by the models exceeded the number actually observed by ~ 20 per cent (we simply assumed 100 per cent field contamination in these bins). Fig. 4 shows the contamination as a function of V magnitude. Note that this figure is somewhat uncertain due to the need to use Galactic models, and especially given the overestimation of the numbers of observed objects by the models, which lends low confidence to the results derived in this section. We therefore pursue an alternative method for obtaining a limit to the contamination level below.

3.2.2 Radial distribution

An alternative method for generating a simple upper limit to the contamination level has also been applied to verify the results obtained

Figure 4. Contamination estimated from Galactic models, measured as the ratio of the calculated number of objects in each magnitude bin from the models, to the number of objects detected and classified as candidate cluster members in that magnitude bin. Note that bins with contamination estimates > 100 per cent (where there were more objects in that bin from the Galactic model than were actually observed) have been truncated to 100 per cent.

Figure 5. Upper limit to the field contamination level estimated from the radial distribution method (see text), plotted as a function of V-band magnitude.

from the Galactic models. Since the cluster is relatively centrally concentrated, we divided the population of candidate cluster members into two bins in radius, using as the centre the position of the star τ CMa. Number counts of objects selected using the CMD as candidate members were then produced inside and outside of a 15 arcmin radius, chosen since it roughly divides the area covered into two, providing good statistics in both bins. By assuming the stars inside 15 arcmin are cluster members, and those outside are not, we can obtain a simple upper limit to the contamination level by dividing these counts, and correcting for the relative area covered by each bin.

Fig. 5 shows the resulting distribution of contamination as a function of magnitude, for comparison with the Galactic model results in Fig. 4. The overall contamination level integrated over all magnitude bins from this method is 68 per cent, comparable to the estimate using the Galactic models from Section 3.2.1.

4 PERIOD DETECTION

4.1 Method

The method we use for detection of periodic variables is described in detail in Irwin et al. (2006), and we provide only a brief summary here. The method uses least-squares fitting of sine curves to the time-series $m(t)$ (in magnitudes) for *all* candidate cluster members, using the form

$$m(t) = m_{dc} + \alpha \sin(\omega t + \phi), \qquad (4)$$

where m_{dc} (the DC light-curve level), α (the amplitude) and ϕ (the phase) are free parameters at each value of ω over an equally spaced grid of frequencies, corresponding to periods from 0.005–50 d for the present data set.

Periodic variable light curves were selected by evaluating the change in reduced χ^2:

$$\Delta\chi_\nu^2 = \chi_\nu^2 - \chi_{\nu,smooth}^2 > 0.4, \qquad (5)$$

where χ_ν^2 is the reduced χ^2 of the original light curve with respect to a constant model, and $\chi_{\nu,smooth}^2$ is the reduced χ^2 of the light curve with the smoothed, phase-folded version subtracted. This threshold was used for the M34 data and appears to work well here too, carefully checked by examining all the light curves for two of the detectors, chosen randomly. A total of 1008 objects were selected by this automated part of the procedure.

The selected light curves were examined by eye, to define the final sample of periodic variables. A total of 271 light curves were selected, with the remainder appearing non-variable or too ambiguous to be included.

4.2 Simulations

Monte Carlo simulations were performed following the method detailed in Irwin et al. (2006), injecting simulated signals of 2 per cent amplitude and periods chosen following a uniform distribution on $\log_{10}$ period from 0.1 to 20 d, into light curves covering a uniform distribution in mass, from 1.2 to 0.1 M$_\odot$. A total of 1015 objects were simulated.

The results of the simulations are shown in Fig. 6 as diagrams of completeness, reliability and contamination as a function of period and stellar mass. Broadly, our period detections are close to 100 per cent complete from 1.2 down to 0.2 M$_\odot$, with remarkably little period dependence. Fig. 7 shows a comparison of the detected periods with real periods for our simulated objects, indicating good reliability.

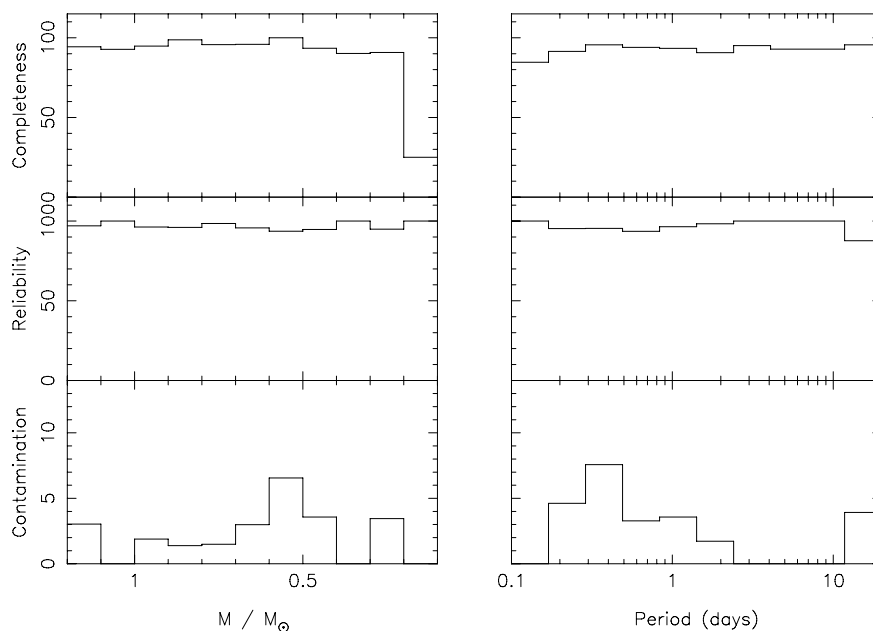## 4.3 Detection rate and reliability

The locations of our detected periodic variable candidate cluster members on a V versus $V - I$ CMD of NGC 2362 are shown in Fig. 8. The diagram indicates that the majority of the detections lie on the single-star cluster sequence, as would be expected for rotation in cluster stars as opposed to, say, eclipsing binaries.

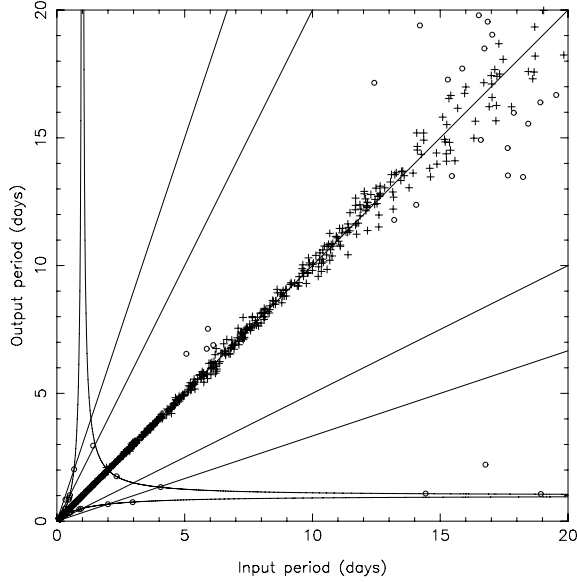The properties of all our rotation candidates are listed in Table 1.

5 RESULTS

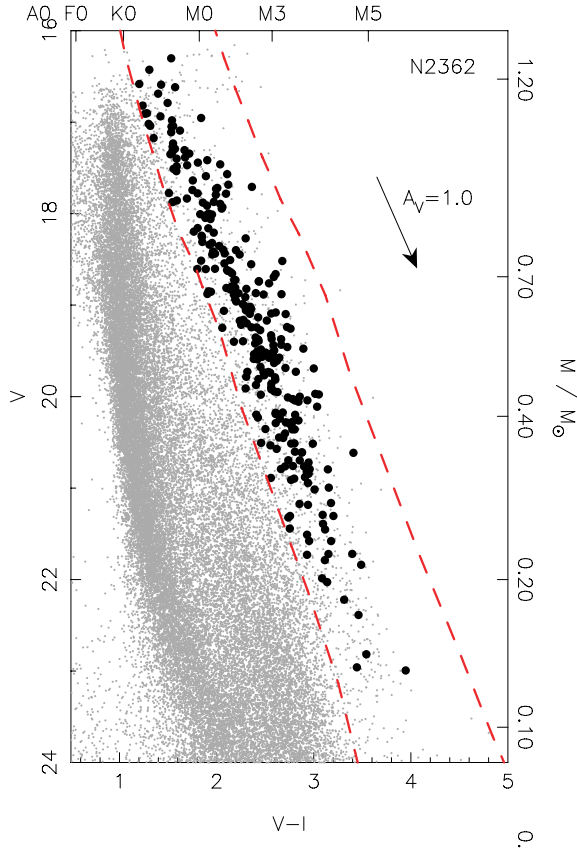## 5.1 NGC 2362 rotation periods

Plots of period as a function of $V - I$ colour and mass for the objects photometrically selected as possible cluster members are shown in Fig. 9. Below $\sim$0.7 M$_\odot$ (or M0), these diagrams reveal a correlation between stellar mass (or spectral type) and the longest rotation period seen at that mass, with a clear lack of slow rotators at very low masses. This trend is also followed by the majority of the rotators in this mass range, with only a tail of faster rotators to $\sim$0.5 d periods, and very few objects rotating faster than this. This

Figure 6. Results of the simulations for 0.02 mag amplitude expressed as percentages, plotted as a function of mass (left-hand panel) and period (right-hand panel). The simulated region covered $0.1 < M/M_\odot < 1.2$ in order to be consistent with the NGC 2362 sample. Top panels: completeness as a function of real (input) period. Central panels: reliability of period determination, plotted as the fraction of objects with a given true period, detected with the correct period (defined as differing by <20 per cent from the true period). Bottom panels: contamination, plotted as the fraction of objects with a given detected period, having a true period differing by > 20 per cent from the detected value.

Figure 7. Detected period as a function of actual (input) period for our simulations. Objects plotted with crosses had fractional period error <10 per cent, open circles >10 per cent. The straight lines represent equal input and output periods, and factors of 2, 3, 1/2 and 1/3. The curved lines are the loci of the $\pm 1\,\mathrm{d}^{-1}$ aliases resulting from gaps during the day. The majority of the points fall on (or close to) the line of equal periods.

Figure 8. Magnified *V* versus *V* − *I* CMD of NGC 2362, for objects with stellar morphological classification, as Fig. 3, showing all 271 candidate cluster members with detected periods (black points). The dashed lines show the cuts used to select candidate cluster members (see Section 3.1).

is very similar to what we found in the earlier NGC 2516 and 2547 studies (Irwin et al. 2007b,c).

Above ∼0.7 M$_{\odot}$, the distribution appears to show little mass dependence, with the slowest rotators all exhibiting ∼10 d periods.

These morphological features do not appear to be a result of sample biases. In particular, the simulations show that the survey is sensitive to much shorter periods than 0.5 d, and the upper limit in detectable periods is not mass dependent, so this cannot explain the sloping morphology of the upper envelope of rotation periods in Fig. 9 at low masses.

Fig. 10 may indicate a slight bias towards shorter periods at low masses, if the distribution of amplitudes in the $0.4 \leqslant M/\mathrm{M}_{\odot} < 1.2$ (top) and $M < 0.4\,\mathrm{M}_{\odot}$ bins was the same, with no counterpart to the small group of objects at periods of ∼ 5–10 d and amplitudes <1 per cent visible in the lower panel. However, the result is not highly significant due to small number statistics in the lower mass bin, and it is possible that these objects may be false positive detections, since at these amplitudes and periods, the effect of light-curve systematics is sometimes difficult to distinguish from real variability.

5.1.1 Period histograms

In order to quantify the morphology of Fig. 9, we have used histograms of the rotation period distributions in two broad mass bins, $0.4 \leqslant M/\mathrm{M}_{\odot} < 1.2$ and $M < 0.4\,\mathrm{M}_{\odot}$, shown in Fig. 11. We have attempted to correct the distributions for the effects of incompleteness and (un)reliability using the simulations described in Section 4.2, following the method used in Irwin et al. (2006). The results of doing this are shown in the solid histograms in Fig. 11, and the raw period distributions in the dashed histograms.

The period distributions in the two mass bins of Fig. 11 show clear differences, with the low-mass stars ($M < 0.4\,\mathrm{M}_{\odot}$) showing a strongly peaked rotational period distribution, with a maximum at ∼0.6–0.7 d, whereas the higher mass stars ($0.4 \leqslant M/\mathrm{M}_{\odot} < 1.2$) show a broader distribution. We applied a two-sided Kolmogorov–Smirnov (KS) test to the corrected distributions to confirm the statistical significance of this result, finding a probability of 4×10^{-10} that the distributions were drawn from the same parent population.

The implication of this result is that the observed morphology in Fig. 9, and in particular the increase of the longest observed rotation period as a function of increasing mass, a trend followed also by the bulk of the rotators, is real and statistically significant.

5.2 Comparison with other data sets

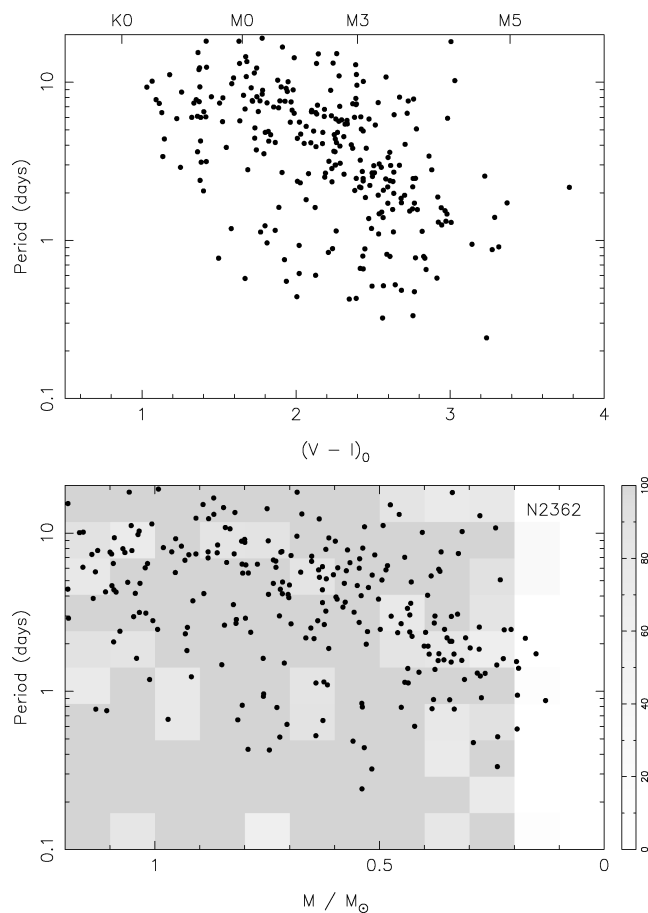#### 5.2.1 Period versus mass diagrams

Fig. 12 shows a diagram of rotation period as a function of stellar mass for the ONC, NGC 2264, 2362, 2547 (∼40 Myr; Naylor & Jeffries 2006) and NGC 2516 (∼150 Myr; Jeffries, Thurston & Hambly 2001). Data sources for each cluster are indicated in the figure caption.

The diagram clearly shows a gradual evolutionary sequence, from a relatively flat mass dependence of the rotation periods in the ONC (∼1 Myr), to a sloping relation in NGC 2264 and 2362, and an increasingly more pronounced slope at the older ages of NGC 2547 and 2516.

The distribution for NGC 2362 appears to show a slightly more pronounced sloping relation than NGC 2264, but the distributions are very similar, indicating that these clusters are close in 'rotational age'. Nevertheless, the rotation period results seem to indicate that

Table 1. Sample of the properties of our 271 rotation candidates, including *V*- and *I*-band magnitudes from our CCD photometry, *Spitzer* IRAC magnitudes in the 3.6, 4.5, 5.8 and 8.0 μm bands, where available, the period *P*, *i*-band amplitude α_i (in units of magnitudes, in the instrumental bandpass), interpolated mass and radius (from the models of Baraffe et al. 1998, derived using the *I* magnitudes). Our identifiers are formed using a simple scheme of the cluster name, CCD number and a running count of stars in each CCD, concatenated with dashes. The full table is available as Supplementary Material to the online version of this article on Blackwell Synergy. Machine-readable copies of the data tables from all the Monitor rotation period publications are also available at http://www.ast.cam.ac.uk/research/monitor/rotation/.

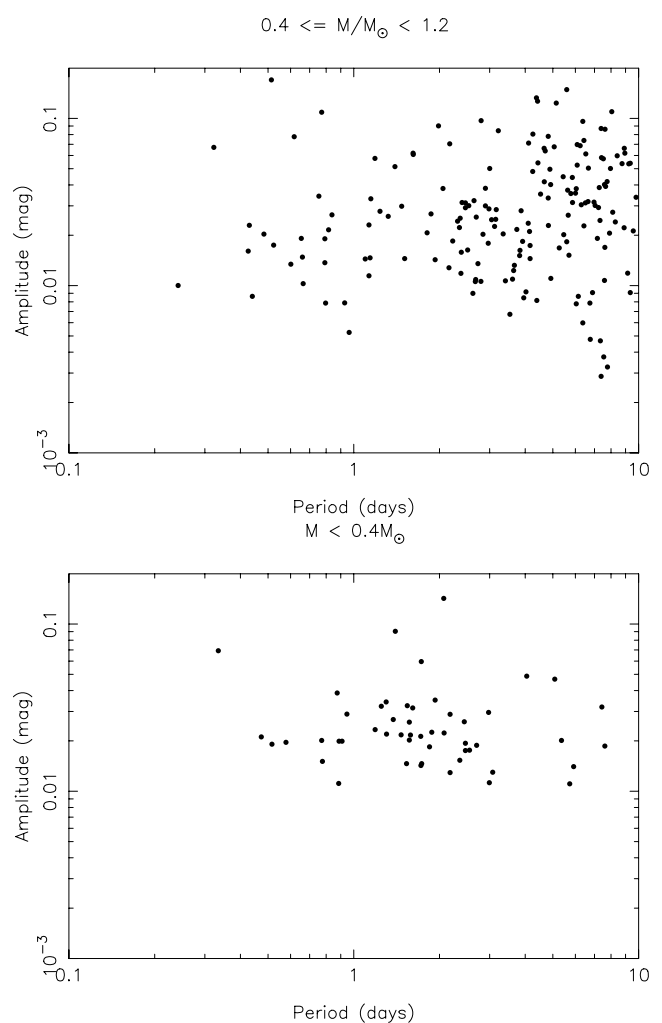| Identifier	RA J2000	Dec. J2000	*V* (mag)	*I* (mag)	[3.6] (mag)	[4.5] (mag)	[5.8] (mag)	[8.0] (mag)	*P* (d)	α_i (mag)	*M* (M$_\odot$)	*R* (R$_\odot$)
N2362-1-1357	07 17 34.82	−25 10 07.0	16.90	15.62					7.344	0.005	1.07	1.70
N2362-1-2076	07 17 39.10	−25 11 32.6	16.91	15.64					7.768	0.003	1.06	1.70
N2362-1-3162	07 17 48.43	−25 13 55.3	21.73	18.80					2.463	0.019	0.19	0.73
N2362-1-4646	07 18 00.08	−25 08 16.3	20.52	17.52					1.141	0.015	0.40	1.08
N2362-1-4685	07 18 00.92	−25 14 24.5	21.31	18.10					10.245	0.014	0.29	0.91

Figure 9. Plots of rotation period as a function of dereddened $V - I$ colour (top), and mass (bottom) for NGC 2362, deriving the masses using the 5 Myr NEXTGEN mass–magnitude relations of Baraffe et al. (1998) and our measured *I*-band magnitudes. In the lower diagram, the grey-scales show the completeness for 0.02 mag periodic variations from the simulations.

Figure 10. Plot of amplitude as a function of period for NGC 2362 in two mass bins: $0.4 \leqslant M/\mathrm{M}_\odot < 1.2$ (top) and $M < 0.4\,\mathrm{M}_\odot$ (bottom).

the canonical age sequence, from youngest to oldest, of the ONC, NGC 2264 and then NGC 2362, is correct.
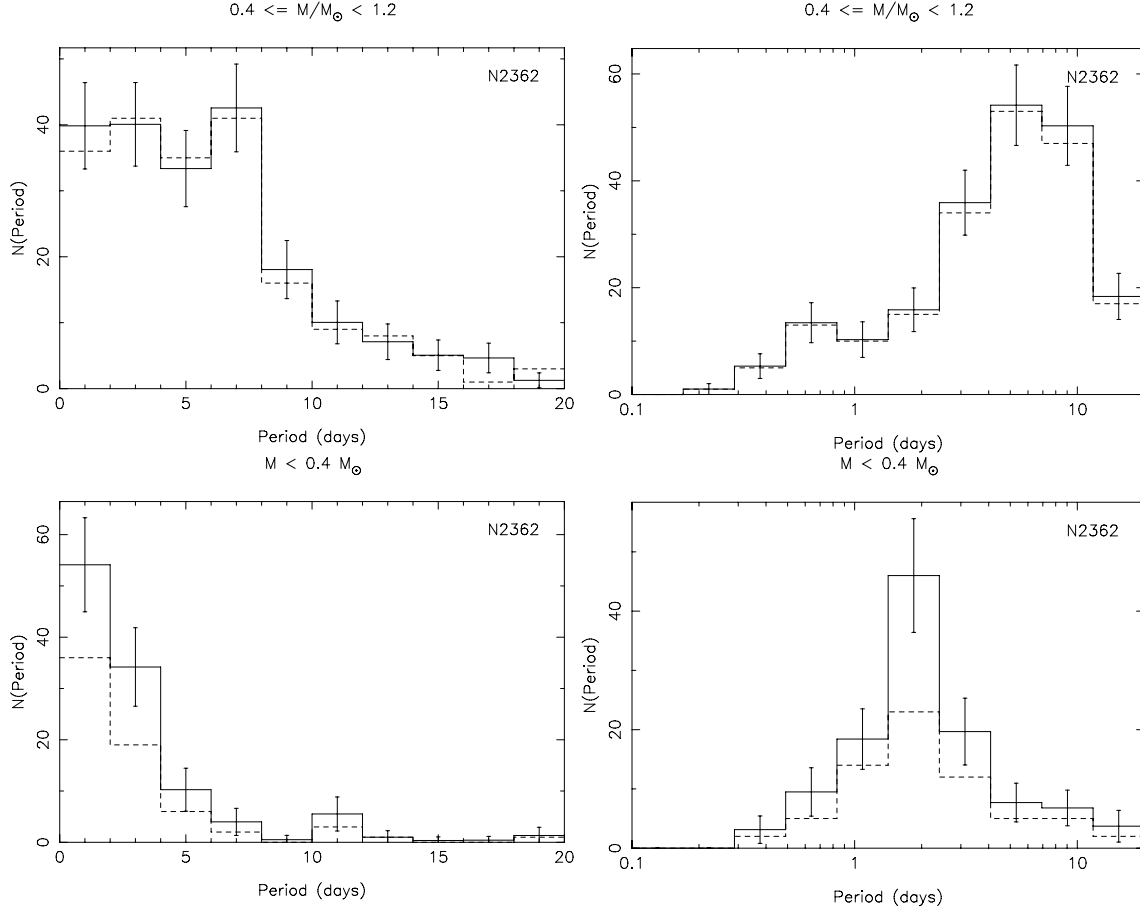
5.2.2 *Comparison with rotational evolution models*

By comparing the observed rotation periods as a function of age with models of rotational evolution on the PMS, we can constrain

the amount of angular momentum loss required during this part of the evolution.

In order to do this, we have used a simple model of solid body rotation from Irwin et al. (2007b), including angular momentum losses due to main-sequence magnetically driven stellar winds (the effect of which is close to negligible during this age range), but

Figure 11. Period distributions for objects classified as possible photometric members, in two mass bins: $0.4 \leqslant M/\mathrm{M}_\odot < 1.2$ (upper row, corresponding roughly to K and early M spectral types) and $M < 0.4\,\mathrm{M}_\odot$ (lower row, late M). The left-hand panels show the distributions plotted in linear period, and the right-hand panels show the same distributions plotted in $\log_{10}$ period. The dashed lines show the measured period distributions, and the solid lines show the results of attempting to correct for incompleteness and reliability, as described in the text.

specifically, not including any additional sources of angular momentum loss ('disc locking' or similar) in order to see if the latter are required to explain the observations. Our models from the earlier NGC 2516 and 2547 work incorporated a simple prescription for core-envelope decoupling, but at these early ages the stars are fully convective, so it is not necessary to incorporate this effect here.

Fig. 13 shows the results of attempting to evolve the measured rotation periods in the ONC forward in time to the age of NGC 2362 using these models.
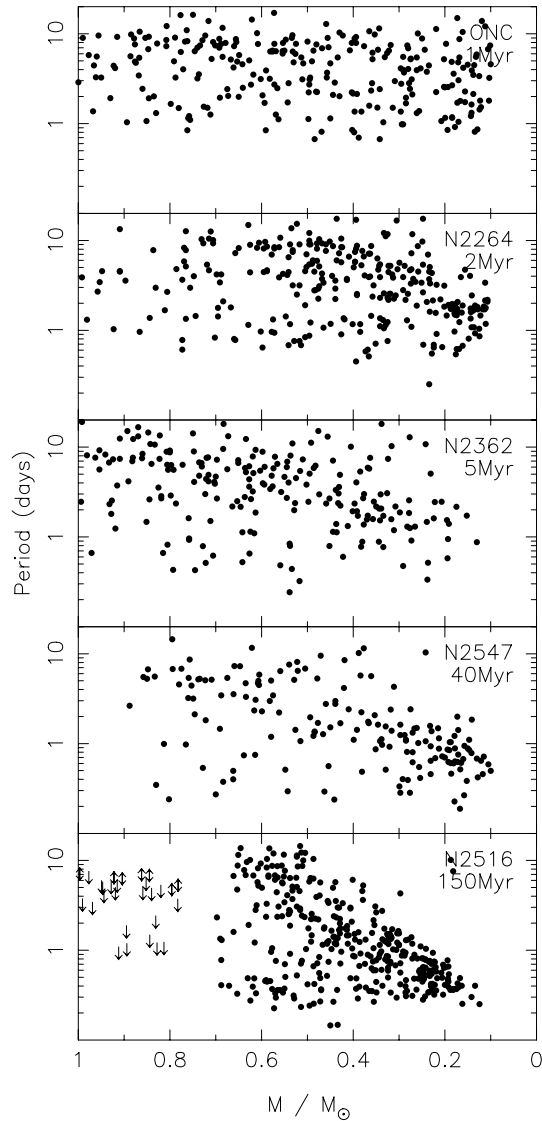
The model clearly cannot successfully reproduce the NGC 2362 distribution. Although there is some hint of the sloping relation at low masses visible in the evolved ONC distribution, the slowest rotators at $M \gtrsim 0.6\,\mathrm{M}_\odot$ are clearly rotating too rapidly. However, the lower envelope of fast rotators is reasonably well reproduced throughout the mass range.

We suspect that the mass determinations (which are based on *I*-band luminosity) are somewhat unreliable in the ONC, due to the presence of strong spatially variable extinction in this cluster. This introduces horizontal scatter in the period versus mass plane. It has been necessary to assume a typical (low) value of this parameter for many of the low-mass detections due to a lack of suitable estimates based on spectroscopy from Hillenbrand (1997). Hence, much of the scatter at low masses in the figure may be due to underestimation of the extinction, and hence of the masses, for highly reddened objects.

However, at the high-mass end, the diagram is more reliable, since the majority of the scatter due to extinction will only move objects to the right-hand side. Therefore, the result that the slowest rotators at these masses are rotating too rapidly is still significant. This indicates that an additional source of angular momentum loss is required, in order to hold the rotation periods of these stars approximately constant (since the slowest rotators in the ONC and NGC 2362 appear to have very similar periods of ~10 d). This is precisely the result found by many other authors, and provides evidence in support of disc regulation, or a similar mechanism, operating over the early PMS stages of the evolution.

We note that the age of the ONC is still a subject of controversy in the literature at the time of writing. Some recent studies (e.g. Sandstrom et al. 2007; Jeffries 2007) have indicated that the distance to the ONC may be ~390 pc, rather than the conventional value of 470 pc used by Hillenbrand (1997). Depending on the PMS evolutionary tracks used, this can raise the derived age to ~2 Myr, which may help to explain these apparent discrepancies. We have explored this further in Fig. 14, which shows the result of assuming a 2 Myr age for the ONC, and evolving the rotation period distribution forward in time. Since the models then predict less spin-up, it is not surprising that the slow rotators at solar mass are better-fit, but still with evidence for (more modest) angular momentum loss being required to fully reproduce the NGC 2362 slow rotator population.
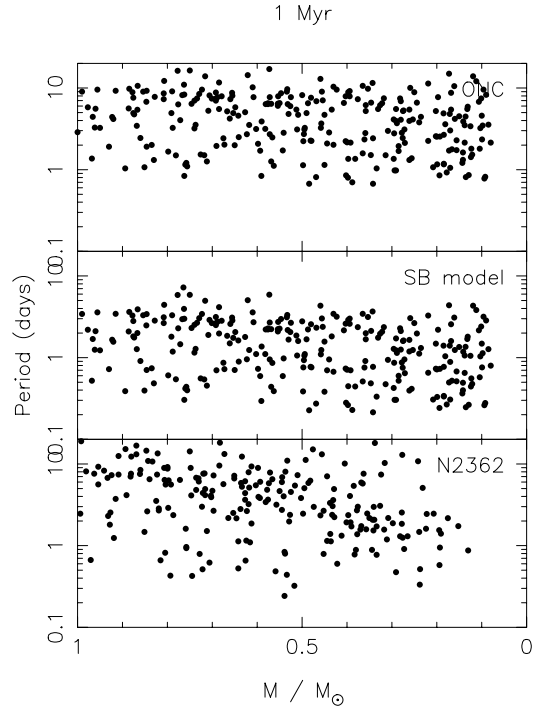
Figure 12. Rotation period as a function of stellar mass for (top to bottom): ONC, NGC 2264, 2362, 2547 and 2516. Lower and upper limits (from $v \sin i$ data) are marked with arrows. The masses were taken from the NEXTGEN mass–magnitude relations (Baraffe et al. 1998) at the appropriate ages. The ONC data are from Herbst et al. (2002). For NGC 2264 we used the data of Lamm et al. (2005) and Makidon et al. (2004). The NGC 2547 and 2516 rotation period data are from the Monitor project (Irwin et al. 2007b,c).
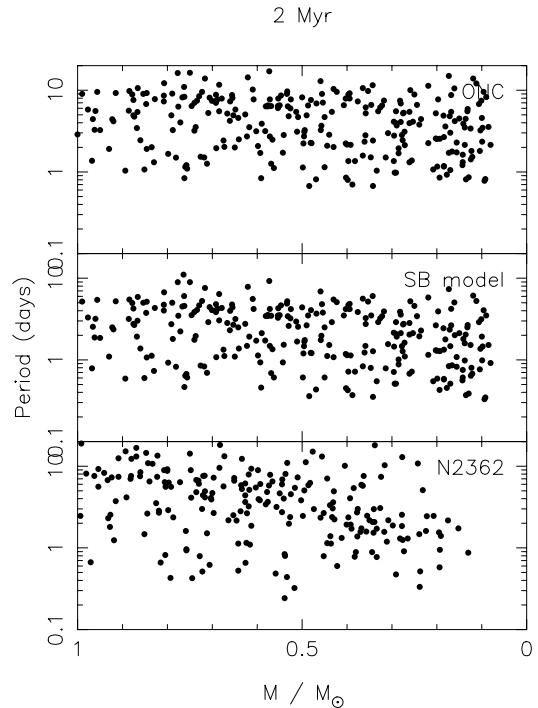
However, at lower masses, the resulting slower rotation for the bulk of these objects places the upper limit to the rotation periods even higher than observed in NGC 2362. Raising the age of the ONC does not therefore readily provide an explanation for the problems at the low-mass end that have already been discussed.

We have also repeated the analysis using NGC 2264 as the initial condition. Fig. 15 shows the results, where we have assumed a 2 Myr age for this cluster. NGC 2264 has much less differentially variable reddening than the ONC, so the low-mass end of the diagram should be more reliably reproduced in this cluster.

The diagram indicates that this is indeed the case, and that the sloping relation for the slow rotators at low masses in NGC 2362 is well reproduced by evolving the NGC 2264 observations forward in time. Again however, the slowest rotators at higher masses
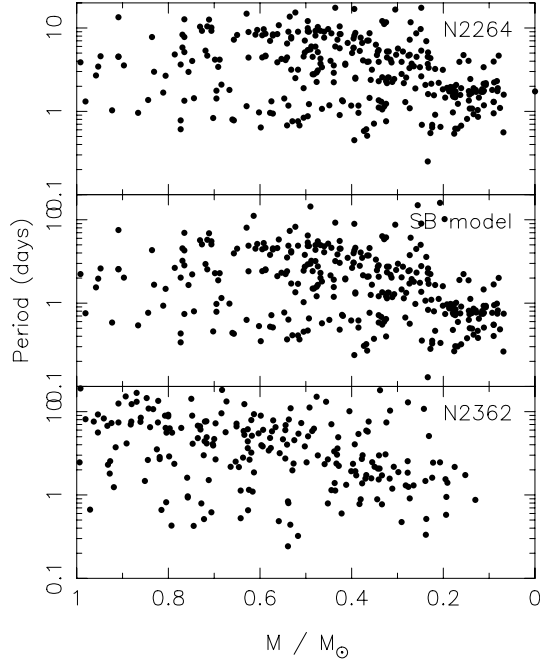

Figure 13. Rotation period as a function of mass, using the model presented in Section 5.2.2 to evolve the ONC distribution (top panel) forward in time from 1 Myr to 5 Myr (middle panel), and the observed NGC 2362 distribution for comparison (bottom panel). Note that these models assume no additional sources of angular momentum loss on the early PMS.

Figure 14. As Fig. 13, except assuming a 2 Myr age for the ONC.

($M \gtrsim 0.6\,M_\odot$) appear to rotate too rapidly compared to the NGC 2362 observations.

Given that these models do not incorporate additional sources of angular momentum loss applying to the early PMS, such as disc

Figure 15. As Fig. 13, except using NGC 2264 as the initial condition, assuming an age of 2 Myr.
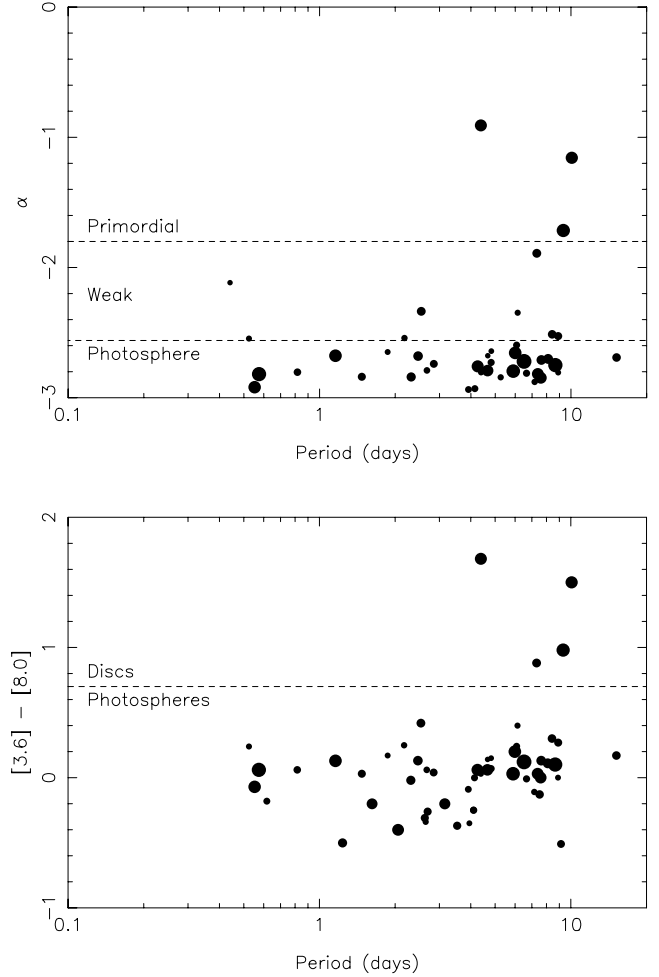
regulation, the ability of the models to reproduce the form of the sloping relation for the lowest mass stars ($M \lesssim 0.5\,\mathrm{M_\odot}$) indicates that these stars do not experience significant angular momentum loss at this stage of their evolution, in contrast to the higher mass stars.

We also demonstrated in our earlier NGC 2516 and 2547 publications (Irwin et al. 2007b,c), that a similar statement applies to the lowest mass stars at later stages in their evolution: even from the ~5 Myr age of NGC 2362 to the ~150 Myr age of NGC 2516, additional angular momentum loss at $M \lesssim 0.5\,\mathrm{M_\odot}$ above that expected due to (saturated) stellar winds does not appear to be required. Given that the higher mass stars do appear to need additional angular momentum losses, this implies that such losses are mass dependent, in the sense that lower mass stars experience less PMS angular momentum loss, or that they lose angular momentum over a shorter time-scale ($\ll 5$ Myr) than the higher mass stars.

5.3 Comparison with mid-IR *Spitzer* observations

In order to search for the correlation between rotation period and the presence of discs expected in the disc regulation paradigm for early PMS angular momentum evolution, we combined the present optical data set with the *Spitzer* IRAC photometry of Dahm & Hillenbrand (2007). Note that Dahm & Hillenbrand (2007) only give mid-IR measurements for objects detected in their combined photometric and spectroscopic survey of the central ~11 × 11 arcmin^2 of the cluster (Dahm 2005), whereas the *Spitzer* FOV is somewhat larger, so this decreases the available sample size. A reanalysis of the *Spitzer* observations to resolve this problem will be attempted in a future publication.

There are 64 stars in common with the catalogue of Dahm & Hillenbrand (2007) which have rotation period measurements. However, in order to obtain a meaningful result, we must restrict the mass range over which the samples are compared: not doing so would introduce a bias at the faint end towards those objects with excesses,
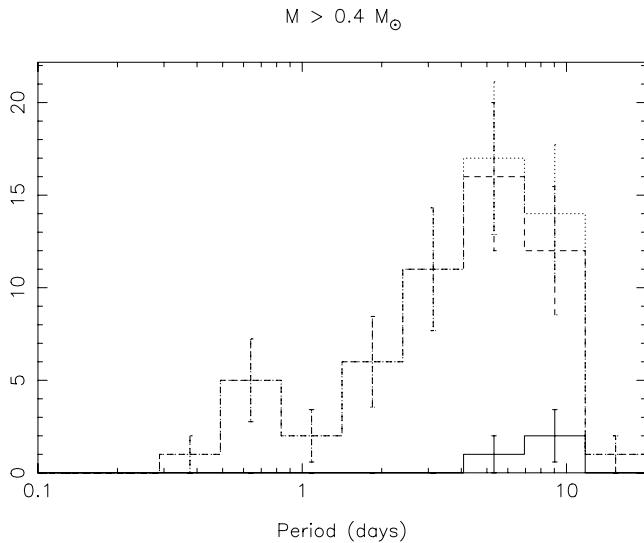

Figure 16. Two disc indicators plotted as a function of rotation period. Symbol sizes indicate the object masses, from $0.4\,\mathrm{M_\odot}$ (smallest symbols) to $1.2\,\mathrm{M_\odot}$ (largest symbols). Top: SED slope α as a function of rotation period. Bottom: $[3.6] - [8.0]$ colour as a function of rotation period. The dashed lines indicate the approximate boundaries in these quantities between regions of the diagram occupied by objects with and without discs, as discussed in the text.

since they are more readily detected in the mid-IR data. Examining fig. 1 of Dahm & Hillenbrand (2007) indicates that the IRAC detection limit is at $[4.5] \simeq 15$, and using the models of Baraffe et al. (1998) for the *M* band (which is a reasonable approximation to the *Spitzer* 4.5 μm band), this corresponds to a conservative limit of $M > 0.4\,\mathrm{M_\odot}$, which has been adopted henceforth.

We have considered two commonly used indicators of the presence of a circumstellar disc: the slope of the IRAC SED, $\alpha = \mathrm{d}\log(\lambda F_\lambda)/\mathrm{d}\log\lambda$, as used by Dahm & Hillenbrand (2007), and the $[3.6]$–$[8.0]$ colour, as used by Cieza & Baliber (2006) and Cieza & Baliber (2007). Fig. 16 shows a plot of these quantities as a function of rotation period.

Thresholds were defined in these quantities, following Dahm & Hillenbrand (2007) for α, with stellar photospheres having $\alpha < -2.56$, 'weak discs' $-2.56 < \alpha < -1.80$ and 'primordial' or optically thick discs $\alpha \geqslant -1.80$. In $[3.6] - [8.0]$ colour, we follow Cieza & Baliber (2007), and use a threshold of $[3.6] - [8.0] > 0.7$ to identify objects with mid-IR excesses indicative of the presence of discs. Fig. 16 clearly indicates that the 'primordial' discs as

M > 0.4 M$_\odot$

Figure 17. Histograms of rotation period for $M > 0.4\,\mathrm{M_\odot}$, showing: objects with IR excesses ('primordial discs', or $\alpha \geqslant -1.80$: solid line), objects without large IR excesses ('weak discs' and 'photospheres', or $\alpha < -1.80$: dashed line), and the entire sample for comparison (dotted line). Poisson error bars are shown.

defined by SED slope, and the excess objects in $[3.6] - [8.0]$, are essentially the same.

Both panels of Fig. 16 indicate that the three to four objects showing strong disc signatures all have long periods, whereas the remainder of the objects show a range of periods, as would be expected in the disc regulation paradigm. This is also seen in distributions of rotation periods in these bins, which are shown in Fig. 17.

Applying a two-sided KS test to the distributions of objects with and without IR excesses gave probabilities of 0.12 (using $\alpha \geqslant -1.80$ to select the objects with significant excesses, corresponding to the 'primordial disc' objects in Fig. 16), and 0.15 (using $[3.6] - [8.0] > 0.7$) that the distributions were drawn from the same parent population. Since the K-S test is not strictly appropriate for such a small sample size, we also considered a simple probabilistic argument: of the 55 objects without excesses, 30 have periods >4 d. The probability that all three objects with excesses were drawn from this same parent population is therefore 0.16. These results indicate that the differences are not statistically significant. This is most likely due to the small sample size.

In spite of this, the distributions do indeed hint at the expected result for the disc regulation paradigm that the objects with discs should be slow rotators, as seen e.g. by Rebull et al. (2006) and Cieza & Baliber (2007). Obtaining a larger sample of objects with rotation period and mid-IR measurements should improve the significance of these results, and allow more definitive conclusions to be made.

6 CONCLUSIONS

We have reported on results of an *i*-band photometric survey of NGC 2362, covering $\sim 0.4\,\mathrm{deg}^2$ of the cluster. Selection of candidate members in a *V* versus $V - I$ CMD using an empirical fit to the cluster sequence found 1800 candidate members, over a *V* magnitude range of $16 < V < 26$ (covering masses from $1.2\,\mathrm{M_\odot}$ down to below the brown dwarf limit). The likely field contamination level was estimated using a simulated catalogue of field objects from the Besançon Galactic models (Robin et al. 2003), finding an overall

contamination level of $\sim$65 per cent, implying that there are $\sim$630 real cluster members over this mass range in our FOV.

We derived light curves for $\sim$85 000 objects in the NGC 2362 field, achieving a precision of <1 per cent per data point over $15 \lesssim i \lesssim 19$. The light curves of our candidate cluster members were searched for periodic variability corresponding to stellar rotation, giving 271 detections over the mass range $0.1 < M/\mathrm{M_\odot} < 1.2$.

The rotation period distribution as a function of mass was found to show a clear mass-dependent morphology, as seen in our earlier NGC 2547, 2516 and M34 studies, and qualitatively similar to that in NGC 2264, which is thought to have a similar age.

Using rotational evolution models from our earlier NGC 2516 work (Irwin et al. 2007b), we were able to show that the distribution of rotation rates for the rapid rotators in NGC 2362 could be reproduced from the distributions in the ONC and NGC 2264 by evolving them forward in time to $\sim$5 Myr. However, for the slow rotators at masses $\gtrsim 0.6\,\mathrm{M_\odot}$, the predicted rotation rates from the models were too rapid, with the observations indicating that the rotation periods of these stars are in fact approximately constant over the $\sim$1–5 Myr age range. This confirms the need for additional angular momentum losses on this part of the PMS, e.g. as would be expected in the disc regulation paradigm.

Finally, we have used the *Spitzer* observations of Dahm & Hillenbrand (2007) to test the disc regulation hypothesis, by searching for a correlation between rotation rate and mid-IR excesses indicative of circumstellar discs. No statistically significant correlation was found with the present small sample sizes, but the three to four objects with significant disc signatures in the sample are indeed all slow rotators.

REFERENCES

Aigrain S., Hodgkin S., Irwin J., Hebb L., Irwin M., Favata F., Moraux E., Pont F., 2007, MNRAS, 375, 29
Baraffe I., Chabrier G., Allard F., Hauschildt P. H., 1998, A&A, 337, 403

Chabrier G., Baraffe I., Allard F., Hauschildt P. H., 2000, ApJ, 542, 464

Cieza L., Baliber N., 2006, ApJ, 649, 862

Cieza L., Baliber N., 2007, ApJ, 671, 605

Dahm S. E., 2005, AJ, 130, 1805

Dahm S. E., Hillenbrand L., 2007, AJ, 133, 2072

Haisch K. E. Jr, Lada E. A., Lada C. J., 2001, ApJ, 553, 153

Herbst W., Bailer-Jones C. A. L., Mundt R., Meisenheimer K., Wackermann R., 2002, A&A, 396, 513

Hillenbrand L., 1997, AJ, 113, 1733

Hodgkin S. T., Irwin J. M., Aigrain S., Hebb L., Moraux E., Irwin M. J., 2006, Astron. Nachr., 327, 9

Irwin M. J., Lewis J. R., 2001, New Astron. Rev., 45, 105

Irwin J., Aigrain S., Hodgkin S., Irwin M., Bouvier J., Clarke C., Hebb L., Moraux E., 2006, MNRAS, 370, 954

Irwin J., Irwin M., Aigrain S., Hodgkin S., Hebb L., Moraux E., 2007a, MNRAS, 375, 1449

Irwin J. et al., 2007b, MNRAS, 377, 741

Irwin J., Hodgkin S., Aigrain S., Bouvier J., Hebb L., Moraux E. 2007c, MNRAS, preprint (arXiv: 0711.0329)

Jeffries R. D., 2007, MNRAS, 376, 1109

Jeffries R. D., Thurston M. R., Hambly N. C., 2001, A&A, 375, 863

Jeffries R. D., Evans P. A., Pye J. P., Briggs K. R., 2006, MNRAS, 367, 781

Königl A., 1991, ApJ, 370, L37

Lamm M. H., Mundt R., Bailer-Jones C. A. L., Herbst W., 2005, A&A, 430, 1005

Landolt A. J., 1992, AJ, 104, L340

Luhman K. L., Stauffer J. R., Muench A. A., Rieke G. H., Lada E. A., Bouvier J., Lada C. J., 2003, ApJ, 593, 1093

Makidon R. B., Rebull L. M., Strom S. E., Adams M. T., Patten B. M., 2004, AJ, 127, 2228

Matt S., Pudritz R. E., 2005, ApJ, 632, 135

Mayne N. J., Naylor T., Littlefair S. P., Saunders E. S., Jeffries R. D., 2007, MNRAS, 375, 1220

Mayor M., 1974, A&A, 32, 321

Miller A., Irwin J., Aigrain S., Hodgkin S., Hebb L., 2008, MNRAS, submitted

Moitinho A., Alves J., Huélamo N., Lada C. J., 2001, ApJ, 563, 73

Naylor T., Jeffries R., 2006, MNRAS, 373, 1251

Park B., Sung H., Bessell M., Kang Y., 2000, AJ, 120, 894

Rebull L. M., Stauffer J. R., Megeath S. T., Hora J. L., Hartmann L., 2006, ApJ, 646, 297

Robin A. C., Reylé C., Derrière S., Picaud S., 2003, A&A, 409, 523

Sandstrom K. M., Peek J. E. G., Bower G. C., Bolatto A. D., Plambeck R. L., 2007, ApJ, 667, 1161

SUPPLEMENTARY MATERIAL

The following supplementary material is available for this article:

Table 1. Properties of our 271 rotation candidates, including *V*- and *I*-band magnitudes from our CCD photometry, *Spitzer* IRAC magnitudes in the 3.6, 4.5, 5.8 and 8.0 μm bands, where available, the period P, i-band amplitude α_i (in units of magnitudes, in the instrumental bandpass), interpolated mass and radius (from the models of Baraffe et al. 1998, derived using the *I* magnitudes). Our identifiers are formed using a simple scheme of the cluster name, CCD number and a running count of stars in each CCD, concatenated with dashes. The full table is available in the electronic edition. Machine-readable copies of the data tables from all the Monitor rotation period publications are also available at http://www.ast.cam.ac.uk/research/monitor/rotation.

This material is available as part of the online article from: http://www.blackwell-synergy.com/doi/abs/10.1111/j.1365-2966.2007.12725.x (this link will take you to the article abstract).

Please note: Blackwell Publishing are not responsible for the content or functionality of any supplementary materials supplied by the authors. Any queries (other than missing material) should be directed to the corresponding author for the article.

This paper has been typeset from a TEX/LATEX file prepared by the author.